Regular Article

Array analysis of seismic noise at the Sos Enattos mine, the Italian candidate site for the Einstein Telescope

Gilberto Saccorotti[1,a] , Carlo Giunchi[1,b] , Michele D'Ambrosio[1,c], Sonja Gaviano[1,2,d], Luca Naticchioni[3,e], Domenico D'Urso[4,5,f] , Davide Rozza[4,5,g], Alessandro Cardini[6,h] , Andrea Contu[6,i], Francesca Dordei[6,j], Matteo Cadeddu[6,k], Matteo Tuveri[6,7,l], Carlo Migoni[6,8,m], Michele Punturo[9,n], Annalisa Allocca[10,13,o], Enrico Calloni[10,13,p], Giovanni Luca Cardello[4,5,q], Luca D'Onofrio[3,r], Nazanin Davari[4,s], Daniele Dell'Aquila[4,5,t], Rosario De Rosa[10,13,u], Massimo Carpinelli[11,5,12,v], Luciano Di Fiore[13,w], Matteo di Giovanni[14,15,x], Luciano Errico[10,13,y], Irene Fiori[12,z], Maria Concetta Tringali[12,aa], Jan Harms[14,15,ab], Soumen Koley[14,15,ac], Vittorio Longo[4,ad], Ettore Majorana[3,16,ae], Valentina Mangano[3,16,af], Marco Olivieri[17,ag], Federico Paoletti[18,ah], Luca Pesenti[4,5,ai], Paola Puppo[3,aj], Piero Rapagnani[3,16,ak], Massimiliano Razzano[18,19,al], Fulvio Ricci[3,16,am], Valeria Sipala[4,5,an], Iara Tosta e Melo[4,5,ao], Lucia Trozzo[13,ap]

[1] Sezione di Pisa, Istituto Nazionale di Geofisica e Vulcanologia, Via Cesare Battisti 53, Pisa, Italy
[2] Dipartimento di Scienze della Terra, Universita degli Studi di Firenze, Florence, Italy
[3] Sezione di Roma, Istituto Nazionale di Fisica Nucleare, Rome, Italy
[4] Department of Chemical, Physical, Mathematical and Natural Sciences, Università degli Studi di Sassari, Sassari, Italy
[5] Laboratori Nazionali del Sud, Istituto Nazionale di Fisica Nucleare, Catania, Italy
[6] Sezione di Cagliari, Istituto Nazionale di Fisica Nucleare, Cagliari, Italy
[7] Dipartimento di Fisica, Università degli Studi di Cagliari, Cagliari, Italy
[8] Osservatorio Astronomico di Cagliari, Istituto Nazionale di Astrofisica, Cagliari, Italy
[9] Sezione di Perugia, Istituto Nazionale di Fisica Nucleare, Perugia, Italy
[10] Dipartimento di Fisica, Università degli Studi di Napoli 'Federico II', Naples, Italy
[11] Dipartimento di Fisica, Università degli Studi di Milano–Bicocca, Milan, Italy
[12] EGO, European Gravitational Observatory, Cascina 56021, Italy
[13] Sezione di Napoli, Istituto Nazionale di Fisica Nucleare, Naples, Italy
[14] GSSI, Gran Sasso Science Institute, 67100 L'Aquila, Italy
[15] Laboratori Nazionali del Gran Sasso, Istituto Nazionale di Fisica Nucleare, L'Aquila, Italy
[16] Dipartimento di Fisica, Universitá di Roma La Sapienza, Rome, Italy
[17] Sezione di Bologna, Istituto Nazionale di Geofisica e Vulcanologia, Bologna, Italy
[18] Sezione di Pisa, Istituto Nazionale di Fisica Nucleare, Pisa, Italy
[19] Dipartimento di Fisica, Università di Pisa, 56127 Pisa, Italy

[a] e-mail: gilberto.saccorotti@ingv.it (corresponding author)

[b] e-mail: carlo.giunchi@ingv.it

[c] e-mail: michele.dambrosio@ingv.it

[d] e-mail: sonja.gaviano@ingv.it

[e] e-mail: luca.naticchioni@roma1.infn.it

[f] e-mail: ddurso@uniss.it

[g] e-mail: davide.rozza@lns.infn.it

[h] e-mail: alessandro.cardini@ca.infn.it

[i] e-mail: andrea.Contu@cern.ch

[j] e-mail: francesca.dordei@cern.ch

[k] e-mail: matteo.cadeddu@ca.infn.it

[l] e-mail: matteo.tuveri@ca.infn.it

[m] e-mail: carlo.migoni@ca.infn.it

[n] e-mail: michele.punturo@pg.infn.it

[o] e-mail: annalisa.allocca@unina.it

[p] e-mail: enrico.calloni@unina.it

[q] e-mail: glcardello@uniss.it

[r] e-mail: ldonofrio@roma1.infn.it

Springer

Abstract The area surrounding the dismissed mine of Sos Enattos (Sardinia, Italy) is the Italian candidate site for hosting Einstein Telescope (ET), the third-generation gravitational wave (GW) observatory. One of the goals of ET is to extend the sensitivity down to frequencies well below those currently achieved by GW detectors, i.e. down to 2 Hz. In the bandwidth [1,10] Hz, the seismic noise of anthropogenic origin is expected to represent the major perturbation to the operation of the infrastructure, and the site that will host the future detector must fulfill stringent requirements on seismic disturbances. In this paper we describe the operation of a temporary, 15-element, seismic array deployed in close proximity to the mine. Signals of anthropogenic origin have a transient nature, and their spectra are characterized by a wide spectral lobe spanning the [3,20] Hz frequency interval. Superimposed to this wide lobe are narrow spectral peaks within the [3,8] Hz frequency range. Results from slowness analyses suggest that the origin of these peaks is related to vehicle traffic along the main road running east of the mine. Exploiting the correlation properties of seismic noise, we derive a dispersion curve for Rayleigh waves, which is then inverted for a shallow velocity structure down to depths of ≈ 150 m. This data, which is consistent with that derived from analysis of a quarry blast, provide a first assessment of the elastic properties of the rock materials at the site candidate to hosting ET.

1 Introduction

Located in the eastern sector of central Sardinia, Italy, the area surrounding the dismissed mine of Sos Enattos is the Italian candidate site for hosting Einstein Telescope (ET), the third-generation gravitational wave (GW) observatory [1, 2]. One of the goals of ET is to extend the frequency band of ground-based GW observations down to the [2,10] Hz interval, where the detector sensitivity can be largely affected by ground vibrations of either natural or anthropogenic origin. Therefore, geodynamical stability and paucity of human activities are of paramount relevance for the evaluation of candidate sites for the construction of ET. Site characterization, with particular reference to seismic disturbances, is thus a necessary step for assessing the potential scientific output of the infrastructure. Within this framework, the Italian National Institute for Geophysics and Volcanology and National Institute for Nuclear Physics (hereinafter referred to as INGV and INFN, respectively) installed three broadband seismometers, one on the surface and the other two at different depths within the principal gallery of the mine. Successively, another seismometer was added to the local network at 160 m below the surface, and all the installations were consolidated. Starting from October 2019, the station located at a depth of 111 m below the surface became part of the networks managed by INGV with the station code SENA (http://cnt.rm.ingv.it/instruments/station/SENA). Previous seismological studies of the Sos Enattos site have been presented in [3–5] and [6]. These results show that the Sos Enattos mine, in the [1,10] Hz frequency band, is classified within the 10% quietest sites among the more than 450 stations present in the database of the Incorporated Research Institutions for Seismology (IRIS). For that same frequency range, the analysis of the underground data highlighted a temporal variability typical of human activity. The most recent work [6]

s e-mail: ndavari@uniss.it

t e-mail: daniele.dellaquila@unina.it

u e-mail: rosario.derosa3@unina.it

v e-mail: massimo.carpinelli@unimib.it

w e-mail: difiore@na.infn.it

x e-mail: matteo.digiovanni@gssi.it

y e-mail: luciano.errico@na.infn.it

z e-mail: irene.fiori@ego-gw.it

aa e-mail: maria.tringali@ego-gw.it

ab e-mail: jan.harms@gssi.it

ac e-mail: soumen.koley@gssi.it

ad e-mail: vlongo@uniss.it

ae e-mail: ettore.majorana@uniroma1.it

af e-mail: valentina.mangano@roma1.infn.it

ag e-mail: marco.olivieri@ingv.it

ah e-mail: federico.paoletti@pi.infn.it

ai e-mail: luca.pesenti@uniss.it

aj e-mail: paola.puppo@roma1.infn.it

ak e-mail: piero.rapagnani@uniroma1.it

al e-mail: massimiliano.razzano@unipi.it

am e-mail: fulvio.ricci@uniroma1.it

an e-mail: vsipala@uniss.it

ao e-mail: itostaemelo@uniss.it
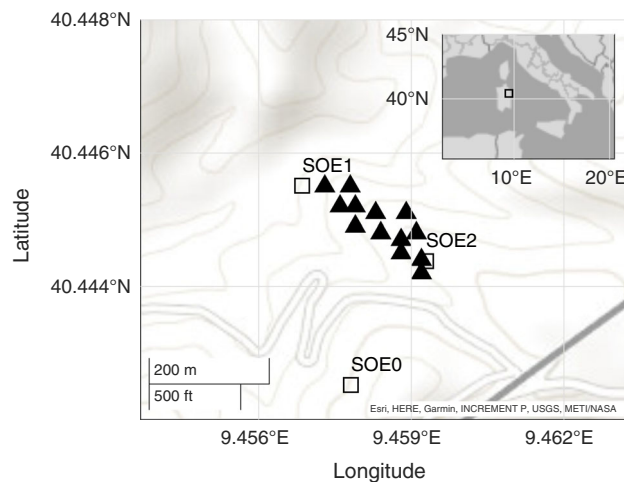
ap e-mail: trozzo@na.infn.it

Fig. 1 Map view of the array deployment (black triangles). The inset shows the location of the study area with respect to Sardinia and peninsular Italy. Squares mark permanent, broad-band stations positioned at the surface (SOE0) and within the mine's tunnel at depths of 84 m (SOE1) and 111 m (SOE2) beneath the surface

analyzes the long-term temporal variation of the seismic noise at Sos Enattos. In brief, results from this latter study indicate that up to a frequency of ≈3 Hz, the main contribution to seismic spectra is that of oceanic microseisms, generally associated with wave climate in the Mediterranean Sea and, occasionally, in the North Atlantic Ocean during strong storms. Above 3 Hz, the spectra of seismic noise reflect the action of both anthropogenic and natural (mostly wind) sources.

In this paper, we make use of a short-period seismic array deployed in proximity of the Sos Enattos mine, to characterize the seismic noise wavefield and to identify its main sources. The paper is structured as follows: first, we introduce the study area and the array experiment. Then, we briefly describe the spectral properties of the seismic noise, and proceed with wavefield decomposition via slowness analysis. Within the anthropogenic frequency band, the noise wavefield is mainly constituted by surface Rayleigh waves associated with vehicle traffic along a main road which runs East of the mine. By exploiting the correlation properties of seismic noise, we derive a dispersion curve which is then inverted for a shallow shear-wave velocity model, which is consistent with that derived from analysis of a quarry blast.

1.1 The study area

The Sos Enattos mine is located in the municipality of Lula, in the Province of Nuoro (central-eastern Sardinia; Fig. 1). The area is characterized by extensive outcrops of the Hercynian basement of Palaeozoic age [7], constituted by low- to medium-grade metamorphic rocks of the pre-Cambrian (?) - Ordovician *pro parte* intruded by late Variscan magmatic rocks. In detail, The Sos Enattos mine is hosted within a crystalline basement of mica schist, quartzite, orthogneiss, and granitoid rocks rich in Sphalerite ([Zn,Fe]S) and Galena (PbS). Exploitation of the mine for the extraction of Lead and Zinc began in 1864, and it lasted until 1996, when the mine was definitively dismissed. Since then, the site has been maintained for dissemination and educational activities. In addition, the mine hosts the SarGrav laboratory, a project involving the construction of both surface and underground facilities dedicated to geophysical and fundamental physics experiments, in a low-noise environment. Within this framework, an experimental verification of energy fluctuations in vacuum is already ongoing [8].

2 Instruments and data

2.1 Instruments

At frequencies above a few Hz, most commercial short-period seismometers exhibit a self-noise which is higher than the noise floor observed at Sos Enattos ([4]; Fig. 2a). As a consequence, although the main interest was focused to frequencies above 1 Hz, we employed more sophisticated, broad-band sensors whose self-noise was appropriate for the noise condition at the site. The experiment was thus conducted using 12 Reftek C130 24-bit data loggers, connected to Nanometrics Trillium Compact 120 sensors, and 3 Nanometrics Centaur 24-bit data loggers, equipped with Nanometrics Trillium Compact 20 PH seismometers. All the data loggers were set in high-gain mode, with full-scale ranges of 1.25Vpp and 1Vpp for the Reftek and Nanometrics digitizers, respectively. The mutual consistency of the different data logger-sensor pairs used for the deployment was carefully checked in a huddle test performed the day before the field installation.
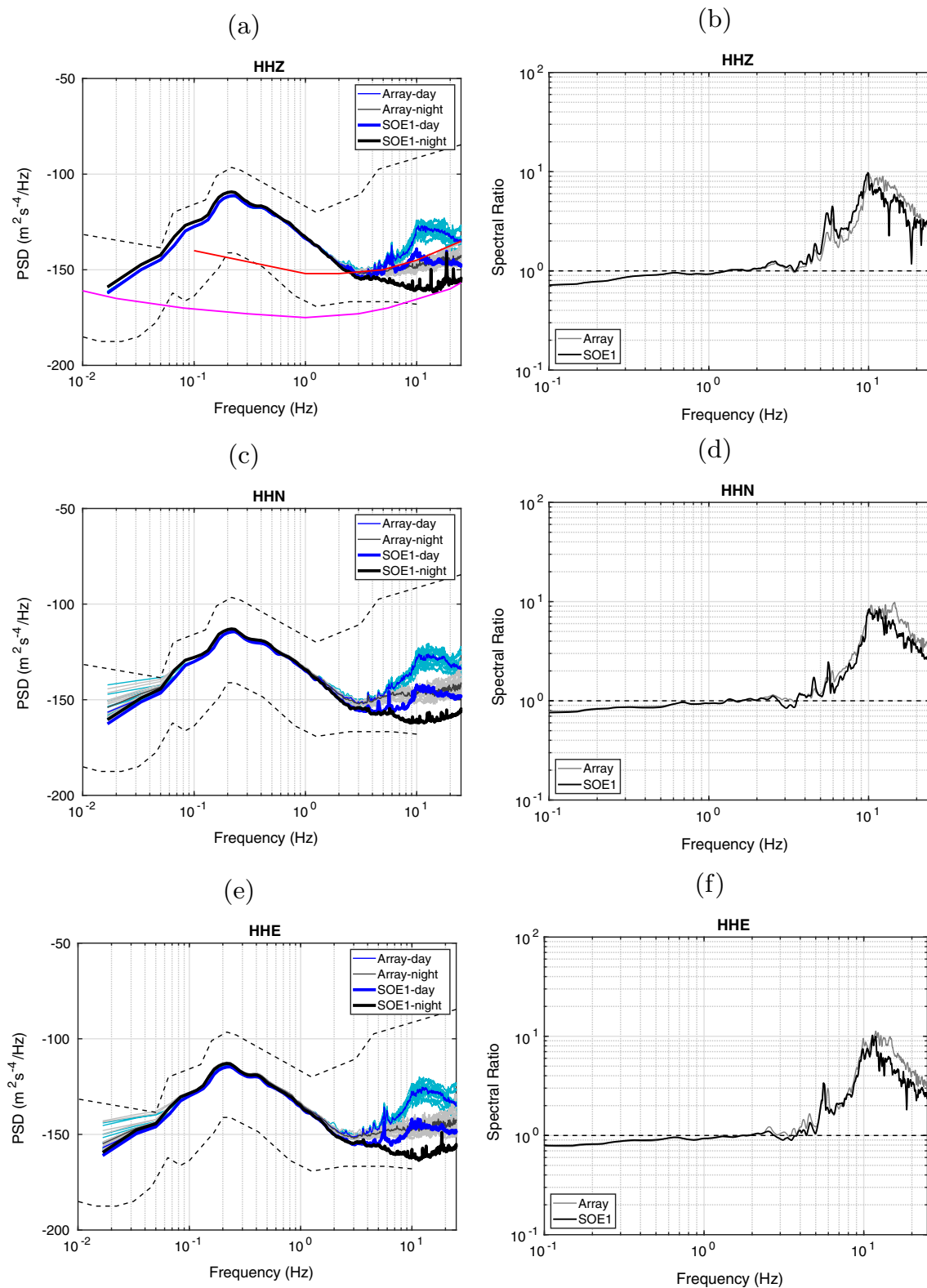
Fig. 2 Typical acceleration power spectral densities (PSD) obtained at the Sos Enattos array for the vertical (**a**), NS (**c**) and EW (**d**) components of ground motion. Cyan and gray lines refer to the PSDs obtained at individual array elements during day and night time-intervals, respectively; thicker lines are the array-averaged spectra. Blue and black lines are the corresponding spectral estimates from underground station SOE1. Dashed black lines indicate the New Low- and High-Noise Models [9]. The red and magenta lines in panel **a** respectively indicate the self noise of Lennartz LE3D-MKIII 1 s and Nanometrics Trillium compact 120 s seismometers. The night- and day-time intervals respectively are 00:00–02:00 UTC and 5:30–7:30 UTC on February 2, 2021 (day-of-year 33). Plots in panels **b**, **d**, **f** show the ratio between the day- and night-time spectral estimates at both the surface array and underground station

2.2 Array design

On the basis of the results obtained from the analyses of both surface and underground data [3, 4], our main goal is to assess the properties of the seismic noise in the anthropogenic frequency band, that is at frequencies above 3 Hz. Di Giovanni et al. [4] estimated phase velocities of Rayleigh waves to range in between 2.5 and 2 km s^{-1} over the [2,5.5] Hz frequency interval. At the target frequency of 5 Hz, the corresponding wavelengths are thus expected to be on the order of 400 m, indicating that an array aperture on the order of 100–200 m should guarantee wavefield coherence throughout the array elements. Further constraints regarded the need to deploy the array above the mine tunnel hosting the underground stations, in turn avoiding too large elevation differences between individual array elements. As a result, the final array geometry was markedly asymmetrical, reflecting the main elongation of the topography (Fig. 1).

2.3 Data

All the stations of the array recorded in continuous mode at a sampling rate of 200 Hz from January 20 to February 5, 2021. On the early morning of January 22, 2021, two stations were set on fire in an act of vandalism; for the rest of this paper, therefore, recordings from those sites are not included.

Data from the surface array are also compared with that from underground station SOE1 (Fig. 1), whose instrumental characteristics are reported in [6].

3 Wavefield analysis

3.1 Spectral properties

Figure 2 shows typical power spectral densities (PSD) evaluated at all the array elements during 2-h-long windows at night and day times. These sample PSDs evidence clearly that the contribution of anthropogenic sources becomes dominant at frequencies above 3 Hz. A clearer picture of the actual contribution of human activities to the noise spectrum is depicted by the panels in the right column of Fig. 2, which show the ratio between the array-averaged PSDs obtained at day and night hours. These plots further confirm that the anthropogenic contribution to the noise spectrum becomes significant at frequencies above a $\approx$ 3 Hz. For comparison, the same calculations have been extended to data from the underground station SOE1, located within a mine gallery beneath the array (see Fig. 1). The attenuation of the spectral power between the surface and underground recordings amounts up to 20 dB, consistently with the factor-10 amplitude decay estimated by [4]. As expected, the day-to-night spectral ratios at the underground site are the same as those estimated at the surface array (Fig. 2, panels b, d, f).

In addition, we observe quite narrow spectral peaks at frequencies 2.5, 4.5, and 6 Hz. Figure 3 illustrates the time- frequency decomposition (spectrogram) for a 1-h-long recording at the vertical components of the array. Energy related to human activities is associated with transient signals; generally, the different frequency bands outlined above appear to be mutually coupled, even if their relative importance varies with time. In particular, the transient wave-trains are characterized by broad spectral lobes spanning the [8, 20] Hz frequency interval, occasionally associated with narrower spectral peaks spanning the [3,6] Hz frequency band.

3.2 Slowness and polarization analyses

Slowness analysis aims at determining the kinematic properties (i.e., apparent velocity and azimuth) with which coherent signals propagate across the array. Under the plane-wave assumption, slowness power spectra are evaluated using the minimum-variance distortionless (or High-Resolution) method developed by [10]:

$$\mathbf{P^{HR}}(\mathbf{S}, \omega_0) = [\mathbf{U}(\mathbf{S})\mathbf{R}(\omega_0)^{-1}\mathbf{U}(\mathbf{S})]^{-1} \qquad (1)$$

where $\mathbf{R}$ is the cross-spectral matrix estimated at angular frequency ω_0, and $\mathbf{U}$ is the beam-steering vector, which contains the phase delays at the different array elements for a plane wave propagating at slowness $\mathbf{S}$. In order to regularize the inversion of the cross-spectral matrix $\mathbf{R}$, a damping factor equal to 5% of the largest eigenvalue of $\mathbf{R}$ is used.

Slowness analysis is conducted following two distinct procedures, both based on a time-frequency decomposition of the array data streams according to 5-s-long time windows sliding with 50% overlap. In the first approach, the spectral covariance (i.e., the elements of the matrix $\mathbf{R}$) is obtained by averaging cross-spectral estimates over the frequency bins spanning a certain frequency interval centered on the reference frequency ω_0. This method is appropriate for analyzing non-stationary signals, whose kinematic properties vary with time. In the second procedure, spectral covariance is derived by averaging over subsequent time windows the spectral coefficients associated with the same frequency bin. This second approach is adopted for measuring the overall dispersive properties of the noise wavefield.

Slowness power spectra (Eq. 1) are calculated over a polar grid of ray parameters p (i.e., the inverse of the modulus of the apparent velocity) and propagation azimuth ϕ. p is measured in s km^{-1}, and ϕ in degrees clockwise from the North direction.
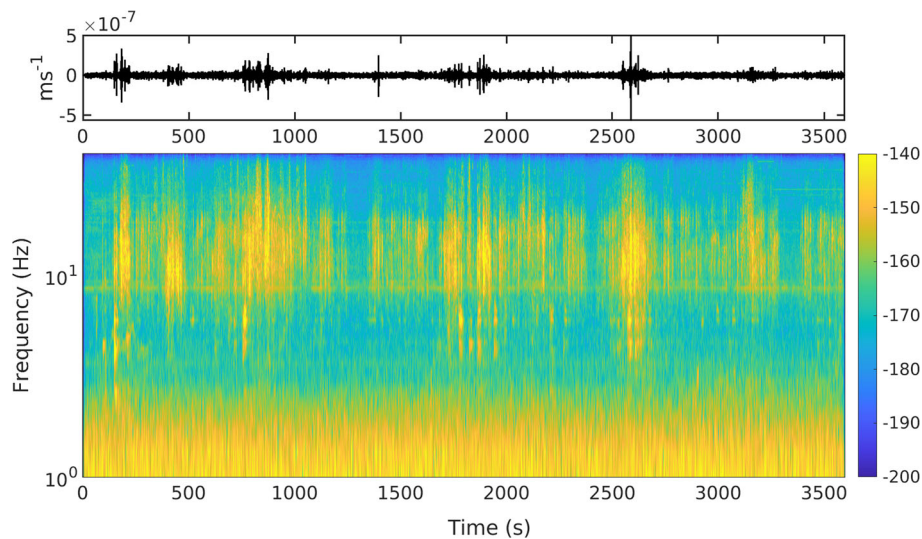
Fig. 3 (top) Sample vertical-component recording of ground velocity at an array station. Data are band-pass filtered over the 1–25 Hz frequency band to better highlight the contribution of cultural noise. At the bottom, the time-frequency representation (spectrogram) of the same signal
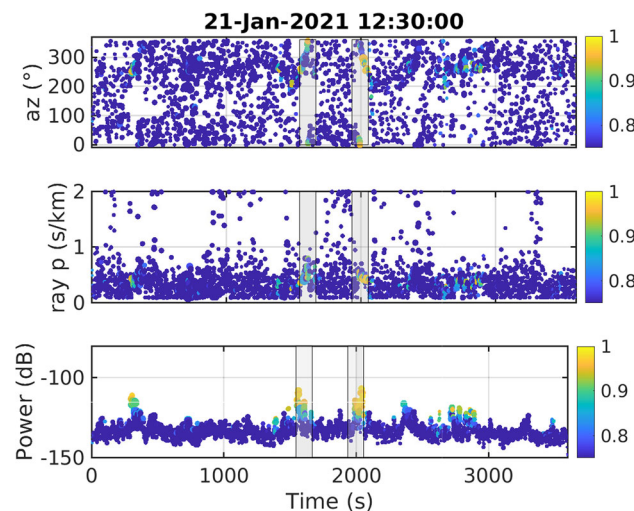

Fig. 4 Propagation parameters for the vertical-component array recordings, over the [5,7] Hz frequency band. From top to bottom, the panels report the propagation azimuth (measured clockwise from the North direction), the horizontal slowness, and the power of the slowness spectrum. Symbols are sized according to the RMS amplitude of the signal, and colored according to the multichannel coherence (see color bars at the right). The two shaded areas indicate the intervals detailed in Fig. 6

Figure 4 illustrates the temporal evolution of propagation parameters for a sample 1-h-long data interval, derived over the [7,11] Hz frequency band. The most energetic and coherent portions of the wavefield are associated with transient pulses propagating from the NE and SE quadrants with ray parameters in the 0.25–0.5 s km^{-1} range, corresponding to apparent velocities between 2 and 4 km s^{-1}.

3.2.1 Vehicle tracking

Figure 5a shows a detail of the wavefield properties associated with one of the largest-amplitude arrivals (see gray areas in Fig. 4). This wave-packet is characterized by horizontal slownesses in between 0.4 and 0.5 s km^{-1}, corresponding to apparent velocities in the 2–2.5 km s^{-1} range. Propagation azimuths exhibit a characteristic drift from about 250° to about 360°, suggesting a source which migrates from East to South of the array. A symmetric behavior is observed in Fig. 5b, in which the propagation azimuths gently drifts from 360° to about 270°, indicative of a source moving from South to East of the array. The most immediate hypothesis about the origin of these signals is that of vehicles traveling along Provincial Route 73 (SP73 hereinafter), which spans the two quadrants East of array. To test this hypothesis, we calculate the azimuths predicted at the array location for a vehicle moving along
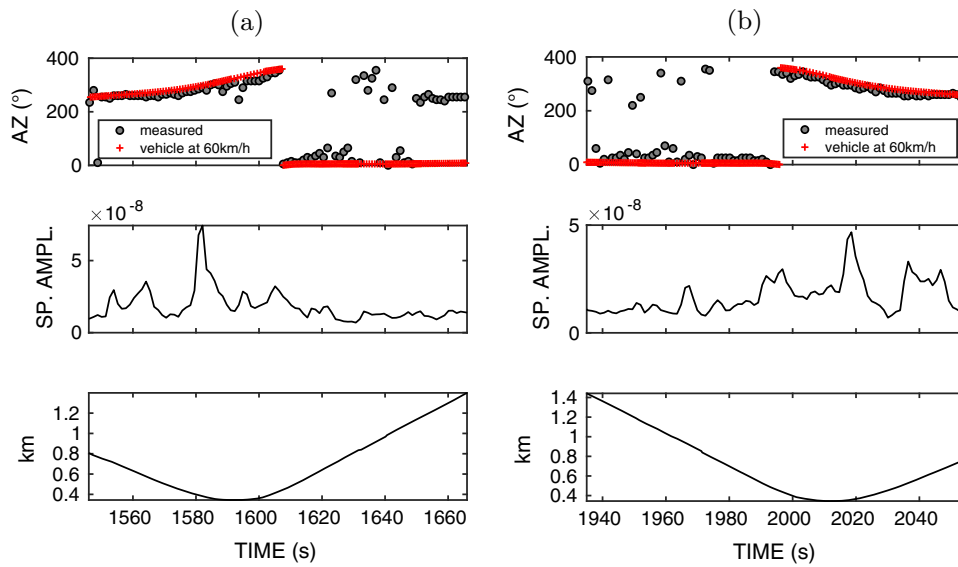
Fig. 5 Propagation azimuths, spectral amplitudes and distance to the source for the two time windows highlighted in Fig. 4. The top two panels report the comparison between the observed azimuths, and those predicted for a vehicle traveling along SP73 from North to South (**a**) or South to North (**b**). Time is relative to the date and time reported at the top of Fig. 4

SP73. A ≈ 7-km-long portion of that road is discretized with N nodes, and either one of the two extreme nodes is considered as the first source activated at time 0. The subsequent sources act at origin times given by

$$T_i^0 = \sum_{j=1}^{i} \frac{dx_j}{v} \tag{2}$$

where dx is the length of the road segment in between two subsequent nodes, and v is the (unknown) vehicle velocity. That signal arrives at the array at time

$$T = T_i^0 + \frac{\Delta_i}{c} \tag{3}$$

where Δ_i is the distance between the i-th node and the baricenter of the array, and c is the propagation velocity of seismic waves, here taken equal to 2.5 km s^{-1} [11]. To simplify the problem, the vehicle velocity v is assumed to be constant, and its most appropriate value is selected after a trial-and-error procedure. For each road node, we calculate the azimuth to the array, and compare it with the propagation direction measured at the corresponding time. Synchronization of the predicted azimuths with slowness measurements is achieved by considering the road locations at which the source-to-receiver azimuth wraps, which are well identifiable on both theoretical and observed data. The two examples reported in Fig. 5 are relative to vehicles traveling from South to North, and vice-versa. In both cases, a vehicle velocity around 60 km per hour provides a reasonable fit of predicted azimuths to the observations. It is worth noting that the largest amplitudes are not necessarily associated with the road segment closest to the array, as one would expect. The analysis is repeated using a narrower (2 Hz) frequency interval centered at the frequency peak around 6 Hz. While the general features of the wavefield remain the same, the propagation azimuths are tightly clustered toward a direction shifted some 30° North of that previously observed (Fig. 6, panels a, c). Figure 6 also illustrates the locations obtained by back-projecting onto the road trace the slowness vectors associated with a multichannel coherence greater than 0.5. More specifically, the two maps report the amplitude-weighted count of measured azimuths in 6° bins. At the center frequency 9 Hz, the dominant propagation directions point to a restricted road segment closest to the array (Fig. 6, panel b). Conversely, at frequency 6 Hz, slowness data point to a bridge located some 1 km ENE of the array. We may thus conclude that, while vehicle traffic along SP73 generates a broad-band noise spanning the [5,20] Hz frequency interval, narrow-band peaks at frequencies around 6 Hz are likely related to bridge vibrations triggered by vehicle transit. This occurrence has been confirmed by [6], who installed geophones at the pillars of the two SP73 bridges closest to the array. By correlating the signals recorded beneath the bridges with those contemporaneously recorded at the mine site, these authors found that several spectral peaks spanning the [2.5,6.7] Hz frequency interval exhibited a significant correlation, thus suggesting that the origin of those peaks was actually related to the eigen-oscillation of the bridge triggered by vehicle transit, similarly to what previously observed at the Virgo Gravitational Wave Observatory in Cascina, Italy [12].

3.2.2 Polarization properties and wave-types

Figure 7 shows the three-dimensional particle motion trajectories for a sample transient associated with vehicle transit along SP73. The largest amplitudes of the signal are associated with elliptical particle motion, whose horizontal projection is roughly
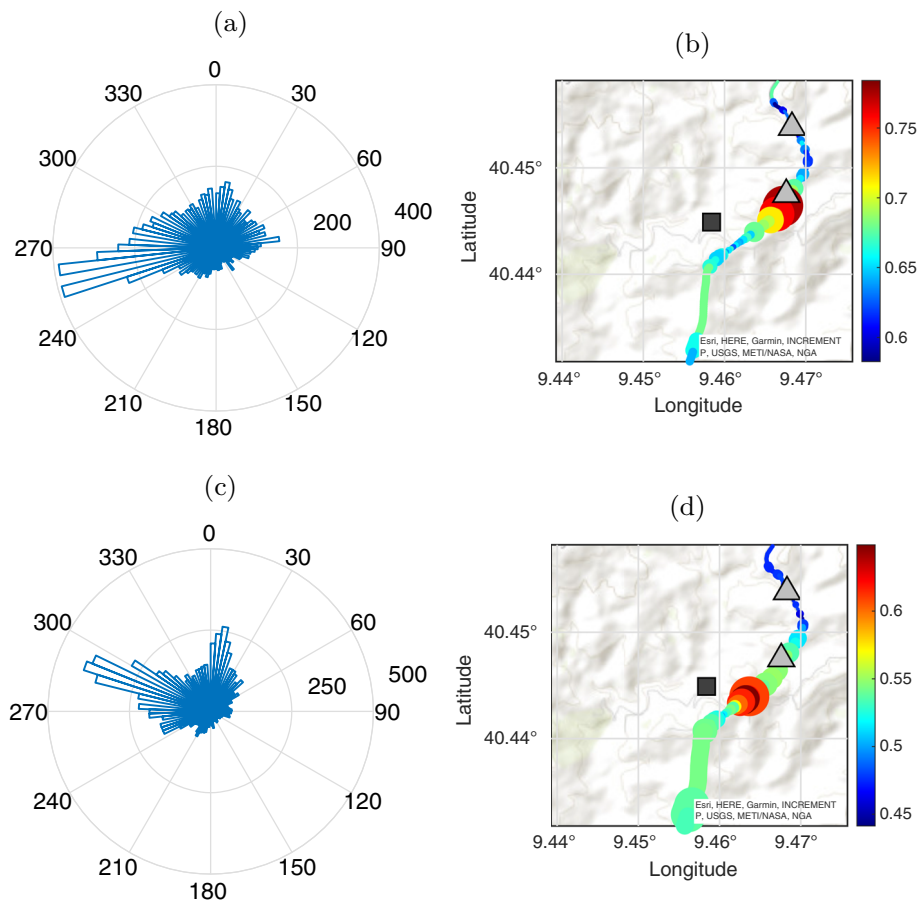
Fig. 6 Rose diagrams **a**, **c** of the propagation directions measured at the Sos Enattos array (gray square). In **b**, **d** location of noise sources along SP73, from back-propagation of slowness vectors. Symbols are sized by the relative frequency of propagation azimuths in 6° bins, weighted for the corresponding amplitude. Colors correspond to the average multichannel coherence, according to the color scale at the right. Panels **a**, **b** and **c**, **d** report the results for the target frequencies of 6 Hz and 9 Hz, respectively. Gray triangles mark the location of two bridges
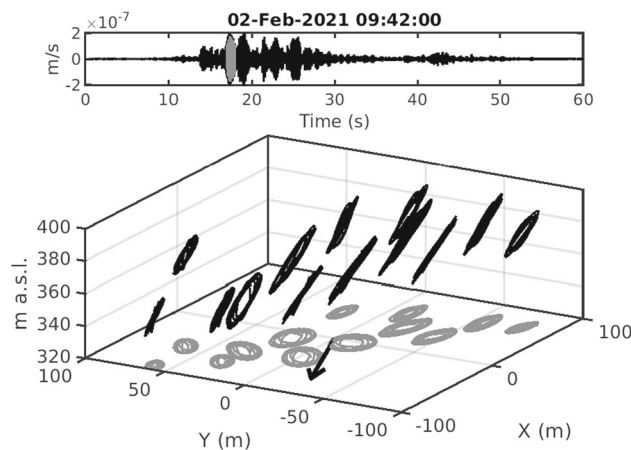
Fig. 7 a Vertical-component seismogram of a sample transient signal associated with vehicle transiting along SP73. **b** Particle motion trajectories for the gray-colored time window in (**a**). Arrow marks the direction of propagation, according to the results from frequency-slowness analyses. Data are band-pass filtered over the 5–7 Hz frequency band

oriented along the direction of propagation. The plane of oscillation, however, is not vertical but tilted some 30° from the vertical. All these characteristics are therefore suggestive of a dominance of Rayleigh waves (radial, elliptical particle motion) propagating in an anisotropic medium. In particular, Rayleigh motion is tilted from the vertical plane when the direction of propagation is perpendicular to the vertical plane of crystal symmetry (see Fig.1 in [13]).
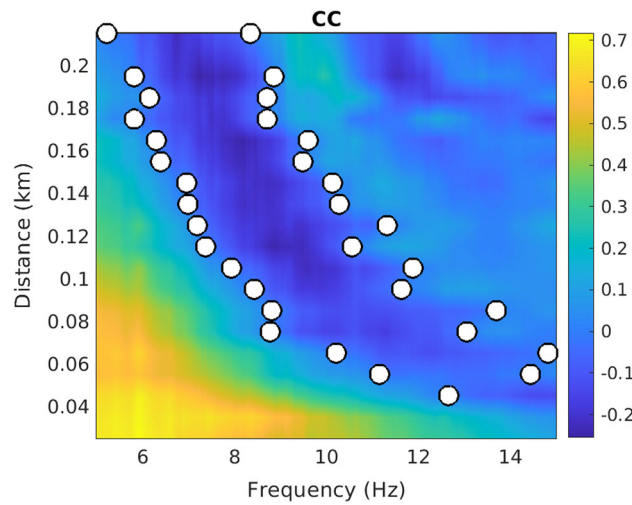
Fig. 8 Spatial Autocorrelation coefficient as a function of frequency and distance. Circles mark the first and second zero-crossings, which are used for estimating Rayleigh-waves phase velocities

3.3 Shallow velocity structure

In this section, we exploit the correlation properties of ambient noise to retrieve the dispersion curve of Rayleigh waves, which is then inverted to derive a shear-wave velocity profile beneath the array.

3.3.1 Spatial autocorrelation (SPAC)

Over the past 20 years, numerous studies used the correlation function of the ambient noise recorded at a pair of receivers in order to determine the propagation velocity of surface waves along the propagation path in between the two recording sites. This class of methods is based upon the correlation properties of stochastic signals, whose first application to seismology date back to the seminal work of Aki [14]. In his study, Aki considered the case of multiple stations located at the same distance but different azimuths with respect to a reference receiver. Under the hypothesis of a horizontally-propagating stochastic wavefield, the azimuthal average of the narrow-band correlation coefficients between the vertical-component seismograms obtained at the reference and peripheral stations is expressed through the relationship [14, eq. 42]:

$$\overline{\rho}(r, \omega_0) = J_0\left(\frac{\omega_0, r}{c(\omega_0)}\right) \tag{4}$$

where $\overline{\rho}$ is the azimuthal average of the correlation coefficients (also termed the spatial autocorrelation) obtained at inter-station distance r and angular frequency ω_0. J_0 is the 0-th order Bessel function, and $c(\omega_0)$ is the phase velocity at frequency ω_0. Thus, by measuring the spatial autocorrelation for a certain r and different values of ω_0, one can obtain the phase velocity dispersion curve at the site for a certain frequency range. The SPAC method was then extended to irregularly-shaped arrays, by averaging the correlation coefficients evaluated for different inter-station azimuths within a finite distance range Δr [15]. Finally, Chavez-Garcia and co-workers introduced the idea that it is possible to substitute an average in time of the correlation in the frequency domain between two stations for the azimuthal average of the correlation computed at that interstation distance [16]. The hypothesis behind this idea is that the average of the cross correlation between a pair of stations for a long enough time window averages all the different directions of the waves composing the microtremors. Thus a single station pair is, in principle, equivalent to an azimuthal average of many station pairs at the same interstation distance.

3.3.2 Dispersion analysis

The first step of SPAC analysis is signal pre-conditioning: the continuous data streams are buffered according to 60-s-long time slices with 50% overlap, which are then detrended, demeaned, tapered, band-pass filtered over the 0.5–20 Hz frequency band. In order to remove the effect of transient, large-amplitude signals of either natural or artificial origin, we apply a running-absolute-mean normalization [17], using an averaging window of length equal to half the maximum period of the filter (i.e., 1 s). Exploiting both the improvements proposed by [15] and [16], frequency-domain cross-correlation estimates are then obtained for all the independent station pairs using 840 subsequent time windows. These correlations functions are finally averaged over time and over sets of station pairs with the same separation distances, with a tolerance of 10 m (Fig. 8). From individual SPAC curves, estimates of phase velocities are finally derived from the two first zero crossings (e.g., [18, 19]), obtaining a dispersion curve spanning the 5–15 Hz
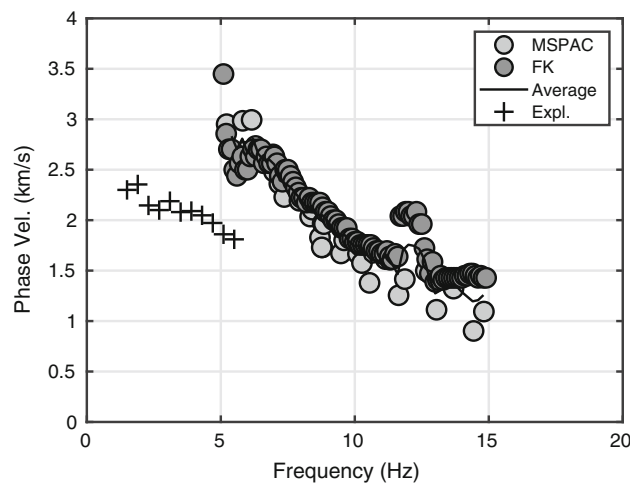
Fig. 9 Dispersion curves derived from the SPAC and frequency-slowness methods (white and gray circles, respectively), and their average (black line). Crosses indicate previous results from analysis of a mine blasting [4]

frequency interval (Fig. 9). These estimates are then compared to those derived from frequency-slowness analysis. Phase velocities derived from the two approaches are mutually consistent, and exhibit a marked dispersive behavior, with values decreasing from 3 km s^{-1} at frequency 5 Hz, to $\approx$ 1 km s^{-1} at frequency 15 Hz. For the [11,14] Hz frequency interval, phase velocities derived from Frequency-Slowness analysis do not respect the overall dispersive trend, and are likely associated with a higher propagation mode. Figure 9 also reports the comparison between these dispersion estimates and the phase velocities presented by [4] from analysis of the recordings associated with a mine blasting fired within the mine.

The dispersion curves shown in Fig. 9 suggest the interference of two distinct Rayleigh-wave propagation modes. Under the assumption that the mine-blasting and noise dispersions are representative of the fundamental and first higher modes, respectively, these two curves are jointly inverted for a shear-wave velocity (Vs) ground profile. The inversion is conducted using the GEOPSY software [20]; the subsurface is parameterized according to three layers of variable thickness overlying a half-space. Density is kept constant at 2600 kg m^{-3}, whereas the Poisson ratio is let to vary in the 0.2–0.3 range. Overall, the results show a good fit between the observed and predicted dispersion curves (Fig. 10). Vs exhibits a marked gradient, ranging from [500, 800] m s^{-1} at the surface up to [2.7,2.9] km s^{-1} at depths of about 110 m. These results depend strongly on the assumption regarding the propagation modes. By neglecting the measurements associated with the mine blasting, and attributing the noise dispersion curve to the fundamental mode, for the same depth range one would obtain velocities about 50% higher.

Pieces of information about the velocity structure at a larger scale are gained from the signals associated with a blast fired in a basalt quarry located some 10 km SE of the mine (Fig. 11a). That explosion was recorded by 9 stations specifically deployed along a linear profile, with inter-station spacings between 750 and 2000 m (Fig. 11b). The distribution of first-arrival times versus distance exhibit a slight slope change, which may be interpreted in terms of the subsequent arrival of direct- and critically-refracted head-waves (Fig. 11c). Under that hypothesis, our data are reasonably fitted by travel-times calculated in a 2-layer model, with a 1-km-thick shallow layer with P-wave velocity around 4.8 km s^{-1}, overlaying a half-space with compressional wavespeed around 5.8 km s^{-1}. Note that the velocities derived for the shallower part are consistent with those derived from the dispersion analysis at depths larger than $\approx$ 120 m (Fig. 11d).

Finally, we test the range of applicability of the shallow velocity model derived from Rayleigh wave dispersion by using that model for locating the quarry blast. The location procedure is conducted by inverting P-wave arrival times manually estimated at the stations of the linear profile, plus station DGI from INGV's monitoring network [21], and borehole stations P2-P3 recently deployed in the frame of ET site characterization efforts (Fig. 11a). The inversion is performed using the probabilistic, non-linear approach by [22, 23]; results are displayed in terms of samples from the *posterior* probability density function projected onto the horizontal plane (Fig. 11a). The maximum likelihood source epicenter is offset by about 1.8 km with respect to the actual blast site, a distance which is compatible with the estimated location uncertainties. As a first approximation, our shallow velocity structure may thus be extended to an area much wider than its original hundreds-of-meters scale.

4 Discussion and conclusions

This paper summarizes the results from the operation of a surface, small-aperture array installed in the vicinity of the Sos Enattos dismissed mine (province of Nuoro, Sardinia). The study is part of the efforts aimed at characterizing the environmental condition of the site, in light of its candidature at hosting Einstein Telescope, the third-generation interferometric detector of gravitational waves. The analyses presented above indicate that most of the anthropogenic noise is associated with vehicle traffic, which manifests
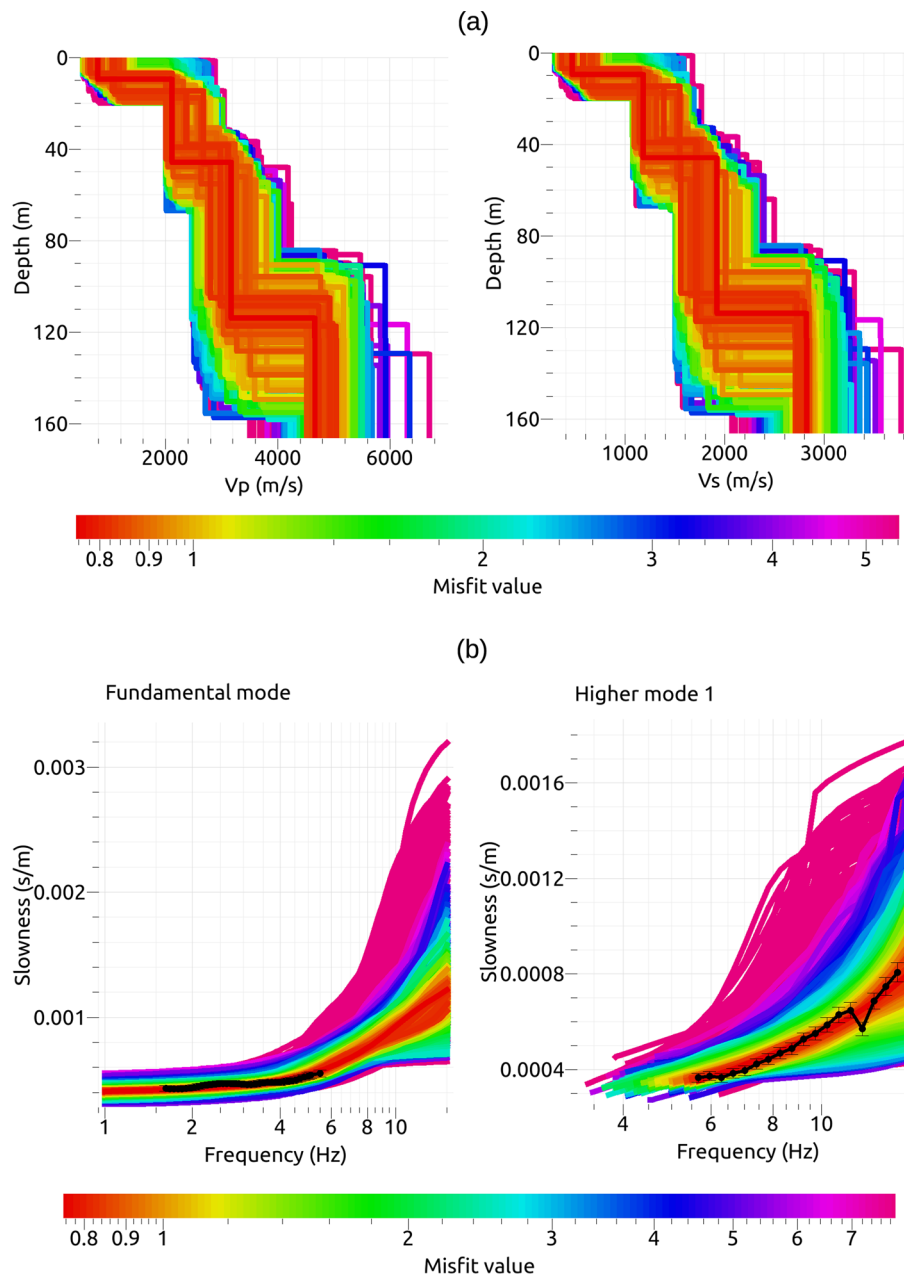
Fig. 10 **a** Compressional- and shear-wave velocity models derived from inversion of the phase velocity dispersions curves shown in Fig. 10. Colors correspond to the inversion misfit, according to the color bar at the bottom. **b** Phase velocities derived from analysis of a mine blasting (left) and from the average of SPAC and frequency-slowness results (right). These curves have been inverted under the hypothesis that they respectively represent the fundamental and first higher mode of Rayleigh waves. Colored lines are the predictions from the set of velocity models investigated during the inversion procedure. As in **a**, colors indicate the inversion misfit according to the colorbar at the bottom

itself in terms of broad-band wavetrains spanning the [3,20] Hz frequency interval, superimposed by narrow-band pulses with characteristic frequencies in the [3,7] Hz frequency band. The kinematic properties of these latter pulses indicate they are most likely generated by the eigen-oscillation of two road bridges. Polarization attributes indicate a dominance of Rayleigh waves, whose vibration planes deviate from the vertical as a consequence of rock anisotropy. Overall, these observations are consistent with previous studies of the seismic signatures of vehicle-induced vibrations, which indicate dominance of Rayleigh waves, and a spectral content mainly restricted to the [2,20] Hz frequency band (e.g., [24]). Under the ET perspective, a crucial subject concerns the establishment of reliable models for predicting the decay of seismic amplitudes at increasing distance from the source. Such predictions are propaedeutic to the definition of respect zones, within which no new noisy infrastructures should be foreseen or activated throughout the lifetime of the detector. Traffic-induced ground disturbances are generated by the different vibration modes of a vehicle triggered by the passage over an irregularity of the road surface, such as a bump. According to observations and numerical
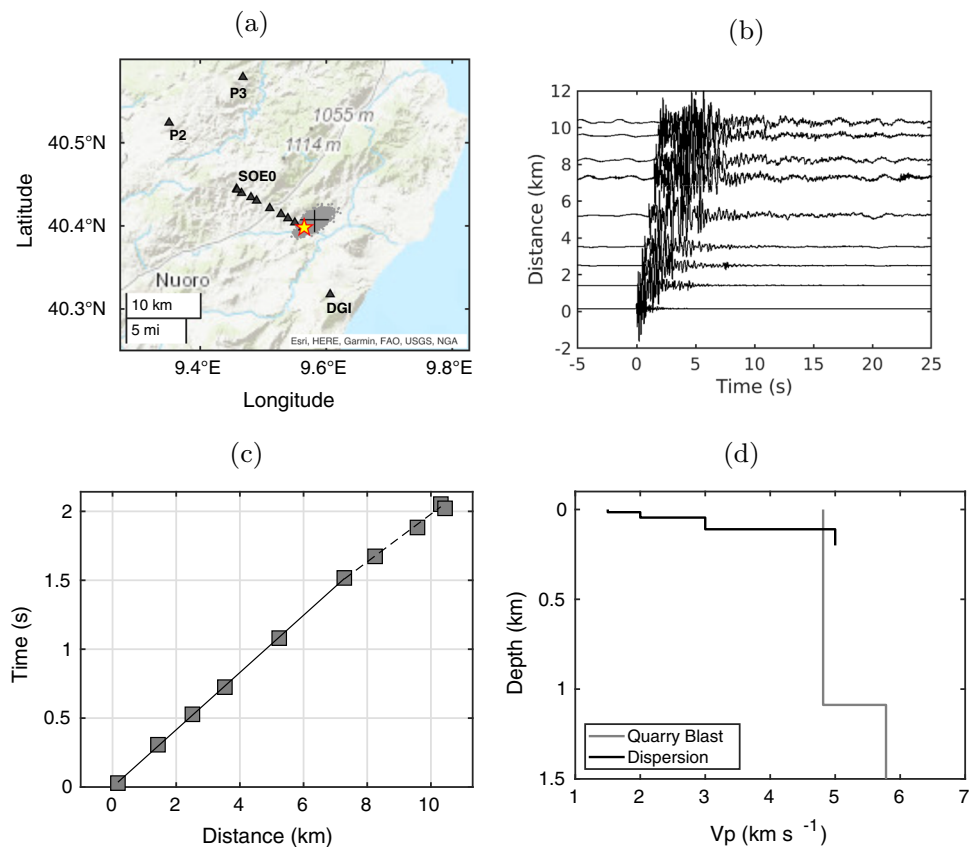
(a)

(b)

(c)

(d)

Fig. 11 a Location of the seismic stations (triangles) used to record the quarry blast fired on January 20, 2022 (star). Station SOE0 is located atop the Sos Enattos mine (see also 1). **b** Record section of the vertical-component seismograms recorded by the stations in (**a**). The time axis is relative to 20 January 2022 at 09:05:11 UTC. **c** P-wave arrival times versus recording distance. A slight slope change is observed at a distance of about 7300 m, which is assumed to represent the cross-over distance beyond which the first arrivals are associated with critically-refracted head waves. **d** 2-layer, P-wave velocity model compatible with the arrival times shown in (**c**). This model is compared with the best-fit velocity structure drived from inversion of Rayleigh-wave dispersion characteristics and illustrated in Fig. 10)

models, the major factors controlling the amplitude of such vibrations are vehicle speed, size and weight, and the scale length of road unevenness (e.g., [25–28]). Therefore, for the same source-to-receiver distance, the disturbance transmitted to the ground depends on the characteristics of the specific vehicles in transit and the scale length of road irregularities, thus implying a large variability of the possible amplitudes at the source. As a consequence, application of any available attenuation model (e.g., [25, 29], and references therein) must be accompanied by a robust statistical assessment of vibration amplitudes observed in proximity of those noisy road segments which may interfere with the future location of ET's infrastructures.

However, ground vibrations from vehicle traffic are an increasingly important environmental issue, for which several mitigation strategies have been developed. These include modifying the ground beneath the road, rather than introducing some form of attenuating barrier beside the road itself. In our specific case, the sources of the largest-amplitude vibrations are very localized in some specific road segments, suggesting that a simple road repavement would likely produce significant beneficial effects. A further mitigation measure consists of local reinforcement of the road's subgrade using stiffening materials, for which both observations and numerical simulations report a decrease in vibration amplitudes of up to 57% [30].

Finally, it must be taken into account that Rayleigh wave amplitude attenuates with depth. For the [1,10] Hz frequency range, we measured phase velocities in between 1.5 and 2.5 km s^{-1} (Fig. 9), thus implying wavelengths λ_R spanning the [150,2500] m interval. For a homogeneous Poisson solid, the vertical-component Rayleigh wave displacement at depths equal to $\lambda_R/2$ is about 60% of that observed at the surface, and basically it vanishes for depths larger than $2\lambda_R$. This data provide constraints on the target depth in case the ET infrastructure should be placed underground.

Data Availability Statement This manuscript has associated data in a data repository. [Authors' comment: The datasets gathered and analysed during the current study are available from the corresponding author on reasonable request. Data of Lennartz and Nanometrics seismometers' self noise shown in Fig. 11a are respectively taken from https://www.lennartz-electronic.de/wp-content/uploads/2021/04/Lennartz-SeismometerManual.pdf and https://nanometrics.ca/hubfs/Downloads/Data%20Sheets/trillium_compact.pdf (last accessed Aug. 8, 2023).].

References

1. M. Punturo et al., The Einstein Telescope: a third-generation gravitational wave observatory. Class. Quantum Gravity **27**(19), 194002 (2010). https://doi.org/10.1088/0264-9381/27/19/194002
2. ET Science Team, Einstein Telescope: science case, design study and feasibility report, https://apps.et-gw.eu/tds/ql/?c=15662 (2020)
3. L. Naticchioni, M. Perciballi, F. Ricci, E. Coccia, V. Malvezzi, F. Acernese, F. Barone, G. Giordano, R. Romano, M. Punturo et al., Microseismic studies of an underground site for a new interferometric gravitational wave detector. Class. Quantum Gravity **31**(10), 105016 (2014). https://doi.org/10.1088/0264-9381/31/10/105016
4. M. Di Giovanni, C. Giunchi, G. Saccorotti, A. Berbellini, L. Boschi, M. Olivieri, R. De Rosa, L. Naticchioni, G. Oggiano, M. Carpinelli et al., A seismological study of the Sos Enattos Area-the Sardinia candidate site for the Einstein Telescope. Seismol. Res. Lett. XX (2020). https://doi.org/10.1785/0220200186
5. A. Allocca, A. Berbellini, L. Boschi et al., Seismic glitchness at Sos Enattos site: impact on intermediate black hole binaries detection efficiency. Eur. Phys. J. Plus **136**, 511 (2021). https://doi.org/10.1140/epjp/s13360-021-01450-8
6. M. Di Giovanni et al., Temporal variations of the ambient seismic field at the Sardinia candidate site of the Einstein Telescope. Geophys. J. Int. **234**(3), 1943–1964 (2023). https://doi.org/10.1093/gji/ggad178
7. L. Carmignani, P. Conti, A. Funedda, G. Oggiano, S. Pasci, La geologia della Sardegna. Geol. F. Trips **4**(2.2), 104 (2012). https://doi.org/10.3301/GFT.2012.04
8. A. Allocca, S. Avino, E. Calloni et al., Picoradiant tiltmeter and direct ground tilt measurements at the Sos Enattos site. Eur. Phys. J. Plus **136**, 1069 (2021). https://doi.org/10.1140/epjp/s13360-021-01993-w
9. J. Peterson, Observations and modeling of seismic background noise. U.S. Geological Survey, Open-File Report 93322 (1993)
10. J. Capon, High-resolution frequency-wavenumber spectrum analysis. Proc. IEEE **57**(8), 1408–1418 (1969)
11. J. Almendros, B.A. Chouet, P. Dawson, Array detection of a moving source. Seismol. Res. Lett. **73**(2), 153–165 (2002). https://doi.org/10.1785/gssrl.73.2.153
12. F. Acernese et al., Properties of seismic noise at the Virgo site. Class. Quantum Gravity **21**(5), S433–S440 (2004). https://doi.org/10.1088/0264-9381/21/5/008
13. S. Crampin, Distinctive particle motion of surface waves as a diagnostic of anisotropic layering. Geophys. J. Int. **40**(2), 177–186 (1975). https://doi.org/10.1111/j.1365-246x.1975.tb07045.x
14. K. Aki, Space and time spectra of stationary stochastic waves, with special reference to microtremors. Bull. Earthq. Res. Inst. **35**, 415–456 (1957)
15. B. Bettig, P. Bard, F. Scherbaum, J. Riepl, F. Cotton, C. Cornou, D. Hatzfeld, Analysis of dense array noise measurements using the modified spatial auto-correlation method (SPAC): application to the Grenoble area. Bollettino di Geofisica Teorica ed Applicata **42**(3–4), 281–304 (2001)
16. F.J. Chavez-Garcia et al., An alternative approach to the SPAC analysis of microtremors: exploiting stationarity of noise. Bull. Seismol. Soc. Am. **95**(1), 277–93 (2005). https://doi.org/10.1785/0120030179
17. G.D. Bensen et al., Processing seismic ambient noise data to obtain reliable broad-band surface wave dispersion measurements. Geophys. J. Int. **169**(3), 1239–60 (2007). https://doi.org/10.1111/j.1365-246X.2007.03374.x
18. I. Cho, S. Senna, A. Wakai, K. Jin, H. Fujiwara, Basic performance of a spatial autocorrelation method for determining phase velocities of Rayleigh waves from microtremors, with special reference to the zero-crossing method for quick surveys with mobile seismic arrays. Geophys. J. Int. **226**(3), 1676–1694 (2021). https://doi.org/10.1093/gji/ggab149
19. G. Ekström, G.A. Abers, S.C. Webb, Determination of surface-wave phase velocities across US Array from noise and Aki's spectral formulation. Geophys. Res. Lett. **36**, L18301 (2009). https://doi.org/10.1029/2009GL039131.10.1029/2009GL039131
20. M. Wathelet, J.-L. Chatelain, C. Cornou, G. Di Giulio, B. Guillier, M. Ohrnberger, A. Savvaidis, Geopsy: a user-friendly open-Source tool set for ambient vibration processing. Seismol. Res. Lett. **91**(3), 1878–1889 (2020). https://doi.org/10.1785/0220190360
21. Istituto Nazionale di Geofisica e Vulcanologia (INGV), Rete Sismica Nazionale (RSN). Istituto Nazionale di Geofisica e Vulcanologia (INGV) (2005). https://doi.org/10.13127/SD/X0FXNH7QFY
22. A. Lomax, J. Virieux, P. Volant, C. Berge-Thierry, Probabilistic earthquake location in 3D and layered models, in *Advances in Seismic Event Location. Modern Approaches in Geophysics*, vol. 18, ed. by C.H. Thurber, N. Rabinowitz (Springer, Dordrecht, 2000). https://doi.org/10.1007/978-94-015-9536-0_5
23. A. Lomax, A. Michelini, A. Curtis, Earthquake location, direct, global-search methods, in *Encyclopedia of Complexity and Systems Science*. ed. by R. Meyers (Springer, New York, 2014). https://doi.org/10.1007/978-3-642-27737-5_150-2
24. D. Coward, D. Blair, R. Burman, C. Zhao, Vehicle-induced seismic effects at a gravitational wave observatory. Rev. Sci. Instrum. **74**, 4846 (2003). https://doi.org/10.1063/1.1614411

25. G.R. Watts, V.V. Krylov, Ground-borne vibration generated by vehicles crossing road humps and speed control cushions. Appl. Acoust. **59**(3), 221–236 (2000). https://doi.org/10.1016/S0003-682X(99)00026-2
26. G. Lombaert et al., Numerical modeling of free field traffic-induced vibrations. Soil Dyn. Earthq. Eng. **19**(7), 473–88 (2000). https://doi.org/10.1016/S0267-7261(00)00024-5
27. G. Lombaert, G. Degrande, Experimental validation of a numerical prediction model for free field traffic induced vibrations by in situ experiments. Soil Dyn. Earthq. Eng. **21**(6), 485–97 (2001). https://doi.org/10.1016/S0267-7261(01)00017-3
28. M. Crispino, M. D'Apuzzo, Measurement and prediction of traffic-induced vibrations in a heritage building. J. Sound Vib. **246**(2), 319–35 (2001). https://doi.org/10.1006/jsvi.2001.3648
29. L. Auersch, Technically induced surface wave fields, part I: measured attenuation and theoretical amplitude-distance laws. Bull. Seismol. Soc. Am. **100**(4), 1528–1539 (2010). https://doi.org/10.1785/0120090228
30. A. Hegde, H. Venkateswarlu, Mitigation of traffic induced vibration using geocell inclusions. Front. Built Environ. **5**, 136 (2019). https://doi.org/10.3389/fbuil.2019.00136